Crystallization and reentrant melting of charged colloids in nonpolar solvents

Toshimitsu Kanai, Niels Boon, Peter J. Lu (□□□), Eli Sloutskin, Andrew B. Schofield, Frank Smallenburg, René van Roij, Marjolein Dijkstra, and David A. Weitz

Phys. Rev. E **91**, 030301 — Published 23 March 2015

DOI: 10.1103/PhysRevE.91.030301

Crystallization and re-entrant melting of charged colloids in nonpolar solvents

Toshimitsu Kanai,[1] Niels Boon,[2] Peter J. Lu (陸述義),[1] Eli Sloutskin,[1] Andrew B. Schofield,[3] Frank Smallenburg,[4] René van Roij,[2] Marjolein Dijkstra,[4] and David A. Weitz[1]

[1]*Department of Physics and SEAS, Harvard University, Cambridge, Massachusetts 02138, USA*
[2]*Institute for Theoretical Physics, Utrecht University, Leuvenlaan 4, 3584 CE Utrecht, The Netherlands*
[3]*The School of Physics, University of Edinburgh, Edinburgh EH9 3JZ, UK*
[4]*Soft Condensed Matter, Debye Institute for Nanomaterials Science, Utrecht University, Princetonplein 5, 3584 CC Utrecht, The Netherlands*

We explore the crystallization of charged colloidal particles in a nonpolar solvent mixture. We simultaneously charge the particles and add counterions to the solution with aerosol-OT (AOT) reverse-micelles. At low AOT concentrations, the charged particles crystallize into body-centered cubic (BCC) or face-centered cubic (FCC) Wigner crystals; at high AOT concentrations, the increased screening drives a thus far unobserved re-entrant melting transition. We observe an unexpected scaling of the data with particle size, and account for all behavior with a model that quantitatively predicts both the re-entrant melting and the data collapse.

Colloidal particles can spontaneously form structures that exhibit long-range ordered states, making them a fascinating system for fundamental studies of crystal phase behavior [1–4]. The majority of studies focus on colloids which model the hard-sphere interaction, a strong repulsion that prevents particles from overlapping, whose range is restricted to contact [5]. Hard-sphere crystallization is driven through purely entropic effects, and the phase behavior is well studied [5–9]. Typically, the colloids used for these studies are sterically-stabilized polymeric particles in non-aqueous solvents, which can match both the density ρ and refractive index n of the particles, enabling confocal microscopy to be used for these investigations. Even earlier studies focused on charged particles, where crystallization is driven by strong long-range repulsive interactions arising from Coulombic charges on the particles [1, 10–22]. These studies were performed on particles in aqueous solvents, which makes charge effects much easier to induce, but precludes index matching, limiting the use of optical techniques except at very low densities. Instead, X-ray scattering studies [23] showed a fascinating phase behavior of Wigner crystals, including a body-centered cubic (BCC) phase at low concentration, and a solid-solid transition to a face-centered cubic (FCC) phase at higher densities [15–18, 24, 25]. It is also possible to induce charge on particles in non-aqeuous solvents through the addition of charge control agents [21, 26–28]. However, in this case, there is strong coupling between the charge on the particle surface and the ions in solution. Charge-induced crystallization should still be expected, although new behavior may also occur as a consequence of this coupling. Nevertheless, these systems have never been investigated experimentally, and the range of potential behavior has not yet been explored.

In this Letter, we investigate the crystallization behavior of colloidal particles in nonpolar solvents. By adding aerosol-OT (AOT) reverse-micelles, we both charge the particles and add ions to the solution. As AOT concentration increases from zero, the system undergoes a first transition from fluid to a charge-stabilized BCC Wigner crystal, and then a second solid-solid transition from BCC to FCC. Further increasing reverse-micelle concentration leads to a surprising behavior: highly-charged particles undergo a re-entrant transition from FCC crystal back to a fluid; the reverse-micelles screen the charge they induce, destroying the Wigner crystals. We observe the same behavior for several different particle sizes and over a wide range of particle volume fractions ϕ below the hard-sphere crystallization boundary. Strikingly, we observe the phase boundaries to collapse onto a single master curve only when the particle size is included explicitly, in contrast to findings in all other systems. To explain these observations, we present a model for the charging effects of the reverse-micelles, and solve the Poisson-Boltzmann equation in a spherical shell to determine the potential and background charge density. Numerical solutions and a mapping onto the one-component plasma model predict the full crystallization phase boundaries, including the scaling behavior. In addition, we present analytic approximations that capture the asymptotic behavior of the boundaries and provide insight into their scaling.

Our experimental system consists of sterically-stabilized polymethylmethacrylate (PMMA) colloidal spheres labeled with nitro-2-1,3-benzoxadiazol-4-yl (NBD) dye and suspended in a solvent mixture of decahydronapthalene (dielectric constant $\epsilon = 2.1$, $\rho = 0.881$ g/mL, $n = 1.48$) and tetrachloroethylene ($\epsilon = 2.5$, $\rho = 1.623$ g/mL, $n = 1.51$) in a mass ratio of 1:1.1. We load suspensions into rectangular glass capillaries (Vitrocom) with inner dimensions $0.1 \times 2 \times 50$ mm. The particles and solvent have sufficiently similar ρ that we do not observe sedimentation for the duration of the experiment, and have sufficiently closely-matched n that we can visualize all particles individually in 3D using a laser-scanning confocal fluorescence microscope (Leica TCS SP5) [29].

We solubilize charge using aerosol-OT (sodium di-2-ethylhexylsulfosuccinate, or AOT), which, above its critical micelle concentration (cmc), forms reverse micelles whose size does not depend on AOT concentration C_{AOT} [30–32]. Neutral reverse-micelles can interact reversibly via a symmetric two-body mechanism to yield two reverse-micelles with opposite charges [28, 33]; the fraction of ionized reverse-micelles χ is about 10^{-5}, independent of C_{AOT}. To quantify the effects of the reverse-micelles on screening of charges, we formulate reverse-micelle suspensions with a range of

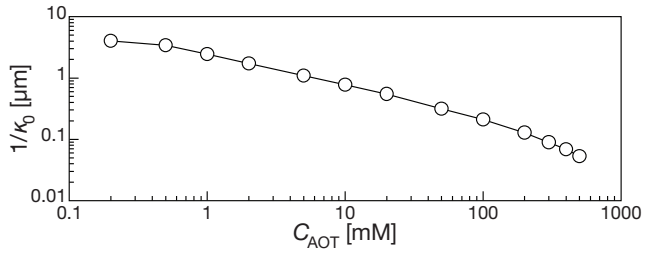

FIG. 1. $1/\kappa_0$ as a function of $C_{\rm AOT}$, determined from conductivity and viscosity measurements.

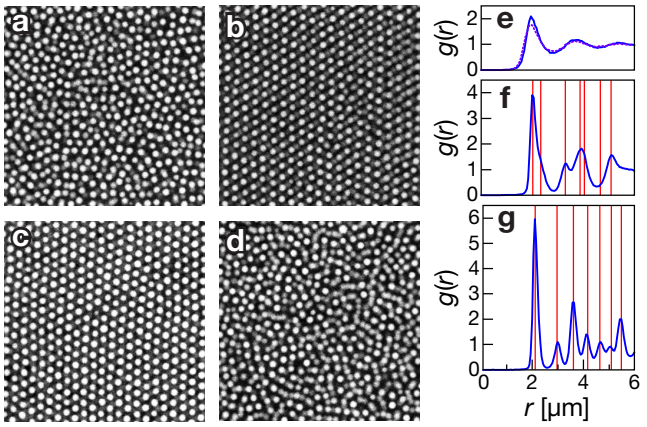

FIG. 2. Confocal microscopy images of PMMA particles at ϕ=0.23 and (a) $C_{\rm AOT}$=1 mM, fluid; (b) $C_{\rm AOT}$=5 mM, BCC crystal; (c) $C_{\rm AOT}$=50 mM, FCC crystal; (d) $C_{\rm AOT}$=200 mM, fluid. (e) $g(r)$ for fluid samples in (a) and (d) shown with dotted purple and solid blue curves, respectively. (f) $g(r)$ for BCC crystal in (b), with major peaks (red lines) corresponding to indices (l. to r.) $\{\frac{2}{3}\frac{2}{3}\frac{2}{3}\}$, $\{100\}$, $\{\frac{1}{2}\frac{1}{2}0\}$, $\{\frac{6}{11}\frac{2}{11}\frac{2}{11}\}$, $\{\frac{1}{3}\frac{1}{3}\frac{1}{3}\}$, $\{\frac{1}{2}00\}$, $\{\frac{6}{19}\frac{6}{19}\frac{2}{19}\}$. (g) $g(r)$ for FCC crystal in (c), with peaks corresponding to $\{110\}$, $\{100\}$, $\{\frac{2}{3}\frac{1}{3}\frac{1}{3}\}$, $\{\frac{1}{2}\frac{1}{2}0\}$, $\{\frac{3}{5}\frac{1}{5}0\}$, $\{\frac{1}{3}\frac{1}{3}\frac{1}{3}\}$, $\{\frac{3}{7}\frac{2}{7}\frac{1}{7}\}$.

$C_{\rm AOT}$; at each concentration, we measure the conductivity σ with an immersion probe (Scientifica), and viscosity η with a glass viscometer (Cannon). From these data, we determine the screening length, $1/\kappa_0 \equiv 1/\sqrt{4\pi\lambda_{\rm B} n_{\rm ion}}$, where the Bjerrum length $\lambda_{\rm B}$ is 24 nm in a solvent with $\epsilon = 2.3$; the total number density of equally-sized monovalent ions is $n_{\rm ion} \equiv 6\pi\eta a_{\rm h}\sigma/e^2$, where e is the elementary charge and a_h is the hydrodynamic radius. We find that the screening length $1/\kappa_0$ decreases monotonically with $C_{\rm AOT}$ [30], as shown in Fig. 1.

To explore the phases that form in these mixtures, we formulate suspensions of the colloidal particles with radius $a = 0.70$ μm at $\phi = 0.23$, and vary $C_{\rm AOT}$ over a wide range. We collect 3D image stacks of these suspensions with a confocal microscope, use software to locate the 3D position of each particle [34–36]. To ensure good statistics, we calculate the 3D pair correlation function, $g(r)$ from at least several thousand particles in each sample. When $C_{\rm AOT} = 0$, the particles are essentially uncharged, and their behavior is well-described as that of a hard sphere fluid; as $C_{\rm AOT}$ increases,

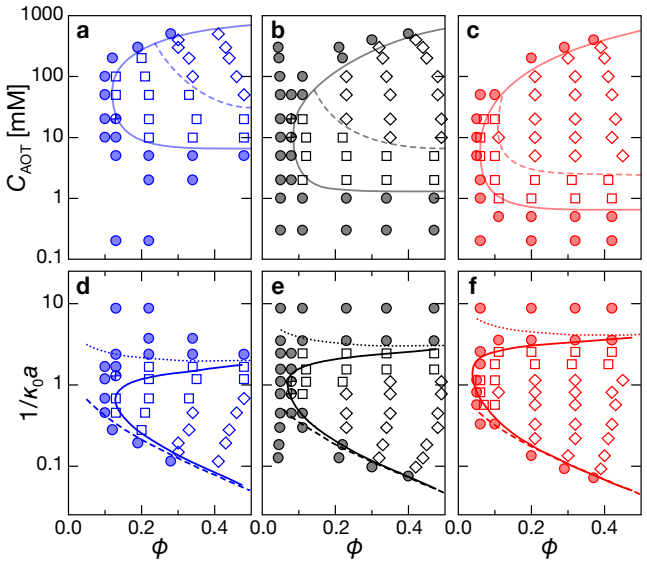

FIG. 3. Phase diagrams for charged crystallization and re-entrance as a function of ϕ and $C_{\rm AOT}$ for particles with (a) $a = 0.46$ μm (blue), (b) 0.70 μm (black), and (c) 0.96 μm (red). Experimentally-determined phases marked with symbols: filled circles (fluid), open squares (BCC), open diamonds (FCC), and semi-filled symbols (fluid-BCC coexistence). Solid curves denote experimental fluid-crystal boundary; solid-solid transition between BCC and FCC marked with dashed curves. (d)-(f) Phase diagrams of the same samples as a function of ϕ and $1/\kappa_0 a$, using the mapping from $C_{\rm AOT}$ to $1/\kappa_0$ in Fig. 1. Solid curves indicate numerical predictions, which closely follow the experimental data. Analytic predictions for the phase boundaries at low- and high-$C_{\rm AOT}$ marked with dotted and dashed lines, respectively.

the particles become increasingly charged leading to correlations between particle positions. For $C_{\rm AOT} = 1$ mM, we observe a strongly-correlated liquid, shown in the 2D confocal image in Fig. 2(a), collected several particle layers from the coverslip, and as with all collected images is representative of the structure throughout the depth of the sample; $g(r)$ for this sample has broad, low peaks, as shown with the dotted purple curve in Fig. 2(e). Upon further increasing $C_{\rm AOT}$, the particles undergo a crystallization transition; at $C_{\rm AOT} = 5$ mM, we observe a disorder-order transition from the fluid to a BCC Wigner crystal, as shown in Fig. 2(b); strikingly, while the particles remain well-separated due to their charge, the order and quality of the BCC crystal lattice is sufficiently high that we can locate and index many of the major peaks in $g(r)$ from the known structure, as shown in Fig. 2(f). Further increasing $C_{\rm AOT}$, we observe a solid-solid crystal phase transition from BCC to FCC structures, shown in Fig. 2(c), and again we can index many of the main $g(r)$ peaks, as shown in Fig. 2(g). Remarkably, however, when $C_{\rm AOT}$ exceeds 200 mM, we observe reentrant melting: the FCC crystal is fluidized, with no crystalline peaks present in $g(r)$, as shown with the blue curve in Fig. 2(e).

To explore more fully the phase behavior of these particles, we repeat the above experiments at several ϕ. The general phase behavior with increasing reverse-micelle concen-

tration, changing from a fluid to BCC to FCC and ultimately to a reentrant fluid, persists over a wide range of ϕ well below the hard-sphere crystal boundary, and for several particle sizes $a = 0.46$, 0.70, and 0.96 μm, as shown with symbols in the phase diagrams in Figs. 3(a)-(c). For sufficiently low $\phi \leq 0.05$, the system remains fluid and does not crystallize anywhere, as shown in the figure. For samples that crystallize at $\phi \approx 0.1$, only the BCC crystal phase is observed; only above $\phi \approx 0.2$ do we observe a clear BCC-FCC phase boundary, which occurs at lower $C_{\rm AOT}$ for increasing ϕ. By contrast, the re-entrant FCC-fluid boundary occurs at higher $C_{\rm AOT}$ as ϕ increases. The qualitative behavior, with the FCC and BCC crystal phases and the re-entrant melting, remains the same for all a, as shown with symbols in Figs. 3(b)-(c).

To explain this behavior, we construct a model that accounts for the basic physical interactions among the micelles and particles at a microscopic level. AOT reverse-micelles affect the particle surface charge through two coupled equilibria. The first reaction is the self-ionization equilibrium of reverse-micelle pairs, described by $2Mic \rightleftharpoons Mic^- + Mic^+$, where *Mic* refers to a neutral reverse-micelle [28]. We characterize this reaction with the constant $K_{\rm M}$, which we use as a fitting parameter. In the bulk, the total ion concentration is: $n_{\rm ion} = [Mic^+] + [Mic^-] = 2\sqrt{K_{\rm M}}[Mic]$. The second reaction is the charging of the colloidal surface through charge exchange of a neutral reverse-micelle *Mic* and a neutral surface site S to form a cationic reverse-micelle Mic^+ and negative surface site S^-: $S + Mic \rightleftharpoons S^- + Mic^+$ [30], characterized by the equilibrium constant $K_{\rm C}$. We assume that the cationic reverse-micelle concentration in the vicinity of the colloid surface, where $r = a$, follows the Boltzmann distribution $[Mic^+]_0 = \frac{1}{2} n_{\rm ion} \exp[-\beta e \psi(r = a)]$ where $\psi(r)$ is the unknown electrostatic potential. We represent the small fraction of charged surface groups f as:

$$f \equiv \frac{[S^-]}{[S]} = \frac{K_{\rm C}[Mic]}{[Mic^+]_0} = \frac{K_{\rm C} \exp(\beta e \psi(r = a))}{\sqrt{K_{\rm M}}} \qquad (1)$$

The total colloidal charge is $Ze = -4\pi a^2 m f e$, where m is the areal density of chargeable surface groups.

To compute Z and $\psi(r = a)$ self-consistently, we calculate the full electrostatic potential $\psi(r)$ in a charge-neutral, spherical Wigner-Seitz cell [37–39] with radius $R = a\phi^{-1/3}$, containing a spherical colloidal particle centered at the origin. On the colloid surface we impose Gauss's law, $\beta e \frac{\partial \psi(r)}{\partial r}\Big|_{r=a} = -Z\lambda_{\rm B}/a^2$. For $a < r < R$ the ionic reverse-micelle concentrations follow Boltzmann distributions $\frac{1}{2} n_{\rm ion} \exp[\pm \beta e \psi(r)]$; we therefore solve numerically the Poisson-Boltzmann (PB) equation of the form:

$$\beta e \frac{\partial^2 \psi(r)}{\partial r^2} + \beta e \frac{2}{r} \frac{\partial \psi(r)}{\partial r} = \kappa_0^2 \sinh[\beta e \psi(r)] \qquad (2)$$

$$\frac{\partial \psi(r)}{\partial r}\bigg|_{r=R} = 0$$

$$\beta e \frac{\partial \psi(r)}{\partial r}\bigg|_{r=a} = 4\pi\lambda_{\rm B} \left(\frac{mK_{\rm C}}{\sqrt{K_{\rm M}}}\right) \exp[\beta e \psi(r = a)]$$

for given $\lambda_{\rm B}$, a, ϕ and κ_0, and for fixed combinations of $mK_{\rm C}/\sqrt{K_{\rm M}}$, which we fit as a single parameter. The calculation yields not only Ze and $\psi(r = a)$, but also the Donnan potential $\psi(r = R)$ and the far-field background ionic charge $\rho_{\rm bg} = -n_{\rm ion} \sinh[\beta e \psi(r = R)]$.

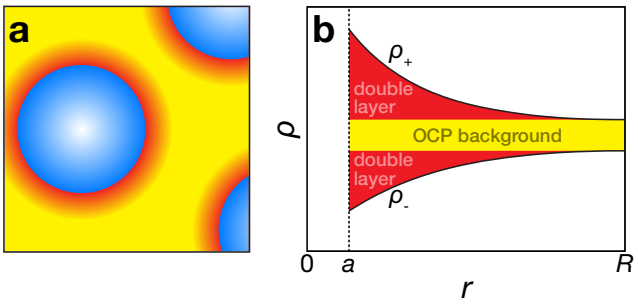

FIG. 4. (a) Illustration of charged particles (blue), their double layers (red), and the OCP background (yellow). (b) Typical ion concentration profiles $\rho_\pm(r)$ around a negatively charged colloidal sphere of radius a in a cell of radius R in the weak-screening regime $\kappa_0 R \lesssim 1$, such that the OCP-like ionic background charge $\rho_+(R) - \rho_-(R) = \rho_{\rm bg}$ (see text) is nonvanishing. By charge neutrality the effective colloidal charge equals $(4\pi/3)(R^3 - a^3)\rho_{\rm bg}$, and the corresponding OCP point-charge is $Z_{\rm OCP} = (4\pi/3)R^3\rho_{\rm bg}$.

To determine where the system crystallizes, we map the colloidal dispersions onto a one-component plasma (OCP) of point particles of density $n \equiv 3\phi/4\pi a^3$ and charge $Z_{\rm OCP} \equiv -\rho_{\rm bg}/n$, to satisfy global OCP neutrality, with a uniform background charge $\rho_{\rm bg}$, as illustrated in Fig. 4. The OCP crystallizes if $\Gamma > 106$ [40, 41] (see appendix), where the OCP coupling parameter is defined as $\Gamma \equiv Z_{\rm OCP}^2 \lambda_{\rm B} n^{1/3}$; this threshold yields a simple new freezing criterion that takes the standard PB cell-model calculations as input. Therefore, to calculate the phase boundaries for comparison with the experimental data, we solve numerically for $\Gamma = 106$ using $\rho_{\rm bg}$, as obtained from the numerical solution of Eq. (2), fitting only the single parameter $mK_{\rm C}/\sqrt{K_{\rm M}} = 5.0 \times 10^2 \mu{\rm m}^{-2}$.

To facilitate comparison between samples, and with theory, we convert the micellar concentration to the dimensionless product $1/\kappa_0 a$, determined by mapping the experimental $C_{\rm AOT}$ to $1/\kappa_0$ via the empirical data in Fig. 1; the experimental data are shown with the symbols in Figs. 3(d)-(f). This representation allows direct comparison between the experimentally-observed phase boundaries, and those predicted by our model. Strikingly, the theoretical predictions are in excellent quantitative agreement with experimental phase boundaries for all a, as shown by the solid curves in Figs. 3(d)-(f). Our new crystallization criterion might be expected to apply only in the low-AOT limit $1/\kappa_0 a > 1$, where the dispersion is OCP-like; however, we observe similar accuracy with the well-established empirical criteria [42–44] for point-Yukawa fluids even for $1/\kappa_0 a < 0.1$. Moreover, our predictions are accurate even at high ϕ; our criterion accounts for the significant hard-core exclusion effects that the ions experience, even as Coulombic repulsion keeps particles well-separated.

The quantitative success of our numerical model suggests

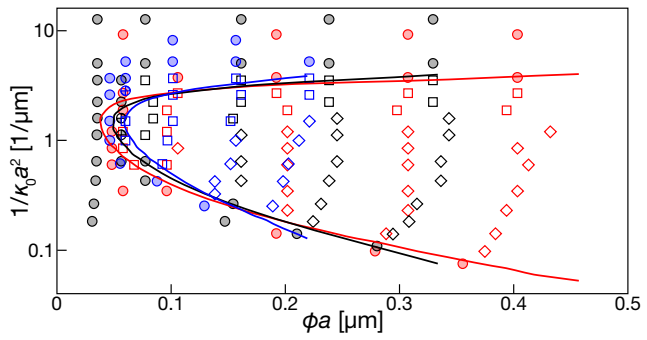

FIG. 5. Phase diagram for all particle radii, with $a = 0.46$ μm (blue), 0.70 μm (black), and 0.96 μm (red), with experimental data and numerical calculations as in Fig. 2, shown as functions of dimensional parameters ϕa and $1/(\kappa_0 a^2)$. All experimental data collapse onto a single behavior (symbols), which is closely modeled by theoretical predictions (curves). Symbols are as in Fig. 3.

that a more analytic approach might also predict accurately the onset of crystallization, in the weak- and strong-screening regimes. For low $C_{\rm AOT}$, the concentration of co-ions is negligible, while the counterions form a uniform background, such that $\rho_{\rm bg} \approx [Mic^+]_0$. Following the described charging equilibrium $Z = -(\kappa_0 a)^2 m K_{\rm C}/(2\sqrt{K_{\rm M}}\lambda_{\rm B}[Mic^+]_0)$ and substituting $Z_{\rm OCP} = Z/(1-\phi)$ in this limit, we obtain the analytic expression

$$\Gamma \approx (4\pi/3)^{2/3}\phi^{-2/3}(1-\phi)^{-1}(\kappa_0 a^2)^2 m K_{\rm C}/2\sqrt{K_{\rm M}} \quad (3)$$

We calculate the phase boundary by determining ϕ and κ_0 where $\Gamma = 106$; remarkably, this yields a predicted phase boundary which converges closely to the numerical calculation and experimental boundary at high-ϕ, as shown with the dotted lines in Figs. 3(d)-(f).

In the concentrated AOT regime, where $1/\kappa_0 a \ll 1$, we assume a small $\psi(r)$ throughout the cell, due to efficient ionic screening. We therefore utilize linear screening theory to find that the general solution to the potential profile is of the form $\psi(r) = A\exp(\kappa_0 r)/r + B\exp(-\kappa_0 r)/r$. We calculate the constants A and B by using cell neutrality and approximate the surface potential to be moderate, $\beta e\psi(a) \approx 1$. The background charge is $\rho_{\rm bg} = -n_{\rm ion}\beta e\psi(R)$. We substitute these into the expression for $Z_{\rm OCP}$, and again use the criterion $\Gamma = 106$ to yield analytical predictions for the re-entrant boundaries. Strikingly, our simple model predicts re-entrance in close quantitative agreement with both the numerical calculations and the experimental data over the entire range ϕ, as marked with the dashed lines in Figs. 3(d)-(f).

Interestingly, the phase boundaries for different a occur at different ϕ and $1/\kappa_0 a$; there is no universal behavior of the data in this dimensionless representation, indicating that particle size plays a non-trivial role. From Eq. 3, at low $C_{\rm AOT}$, Γ depends only on $\kappa_0 a^2$ and ϕ; the ϕ-dependence is weak, featuring a shallow minimum at $\phi = 0.4$, but is roughly constant, consistent with the nearly-constant $C_{\rm AOT}$ observed for this boundary in the experimental data. By contrast, at high $C_{\rm AOT}$ and close to the phase boundary, Γ shows very little remaining dependence on a, when expressed as a function of $\kappa_0 a^2$, ϕa, and a. These mathematical properties suggest that the systems with different a may behave in the same way, when their phases are plotted as functions of the *dimensional* parameters $1/(\kappa_0 a^2)$ and ϕa.

To test this, we re-plot all the experimental data, as functions of $1/(\kappa_0 a^2)$ and ϕa; remarkably, all of the experimental data from all three a collapse onto a universal phase diagram, with the same onset of crystallization and re-entrance for all samples, shown with symbols in Fig. 5. Our theoretical model predicts this boundary, as shown by the overlapping solid curves in Fig. 5. That the collapse occurs when the data are plotted as a function of parameters that explicitly include a length scale, as opposed to the dimensionless case, is particularly striking; moreover, our numerical calculations suggest that this non-dimensionless scaling should apply over a larger range of a, extending over half an order of magnitude beyond the particle sizes used in these experiments. However, the origin of this dimensional data collapse remains an open question.

The excellent agreement between the assumptions of our theoretical model and our experimental data suggests that the same mechanism may drive electrostatically-induced phase transitions in general. Although crystallization curves are fitted accurately, the observed BCC-FCC transition curves cannot be reproduced within our approach, as the OCP does not show FCC ordering. Nevertheless, our model can now be used to predict a wide range of behaviors in charged particle systems, and the flexibility and extended length scales possible through the use of non-polar solvents make these an attractive model system for the study of other phase behavior.

ACKNOWLEDGMENTS

T. K., N. B. and P. J. L. contributed equally to this work. This work was supported by NASA (NNX13AQ48G), the NSF (DMR-1310266 and DMR-1206765), the Harvard MRSEC (DMR-0820484), and JSPS Postdoctoral Fellowships for Research Abroad, and is part of the D-ITP consortium, a program of the Netherlands Organisation for Scientific Research (NWO) that is funded by the Dutch Ministry of Education, Culture and Science (OCW).

APPENDIX

The Coulomb coupling parameter Γ plays a pivotal role in characterisation of one-component plasmas (OCP), and is defined as the Coulomb interaction energy expressed in units of the thermal energy kT for two particles at a typical interparticle distance D: $\Gamma \equiv Z^2\lambda_{\rm B}/D$, where Z is the particle charge. Here we define $D \equiv n^{-1/3}$, where n the particle density, consistent with recent studies [42]. However, other pioneering studies on OCP freezing [40, 41] use a slightly different definition of the interparticle distance, $D^* \equiv (4\pi n/3)^{-1/3}$; this results in a small change to the coupling parameter definition: $\Gamma^* \equiv Z^2\lambda_{\rm B}/D^* \approx 1.61\Gamma$. These studies show that a

Coulomb lattice is the most favourable configuration when the coupling parameter exceeds a critical value, $\Gamma^* \simeq 171$ [41]. Consequently, in our study, the phase transition between the fluid and crystal should occur very close to $\Gamma = 106$; we use this criterion to construct our phase diagrams.

[1] U. Gasser, E. R. Weeks, A. Schofield, P. N. Pusey, and D. A. Weitz, Science **292**, 258 (2001).
[2] A. Yethiraj and A. van Blaaderen, Nature **421**, 513 (2003).
[3] P. Schall, I. Cohen, D. A. Weitz, and F. Spaepen, Science **305**, 1944 (2004).
[4] P. Schall, I. Cohen, D. A. Weitz, and F. Spaepen, Nature **440**, 319 (2005).
[5] A. Kose and S. Hachisu, Journal of Colloid and Interface Science **46**, 460 (1974).
[6] B. J. Alder, W. G. Hoover, and D. A. Young, The Journal of Chemical Physics **49**, 3688 (1968).
[7] P. N. Pusey and W. van Megen, Nature **320**, 340 (1986).
[8] W. K. Kegel and A. van Blaaderen, Science **287**, 290 (2000).
[9] J. L. Harland and W. van Megen, Phys. Rev. E **55**, 3054 (1997).
[10] S. Hachisu, Y. Kobayashi, and A. Kose, Journal of Colloid and Interface Science **42**, 342 (1973).
[11] A. Kose, M. Ozaki, K. Takano, Y. Kobayashi, and S. Hachisu, Journal of Colloid and Interface Science **44**, 330 (1973).
[12] S. Hachisu and Y. Kobayashi, Journal of Colloid and Interface Science **46**, 470 (1974).
[13] B. J. Ackerson and N. A. Clark, Physical Review Letters **46**, 123 (1981).
[14] P. Pieranski, Contemporary Physics **24**, 25 (1983).
[15] D. Hone, S. Alexander, P. M. Chaikin, and P. Pincus, The Journal of Chemical Physics **79**, 1474 (1983).
[16] K. Kremer, M. O. Robbins, and G. S. Grest, Physical Review Letters **57**, 2694 (1986).
[17] W. Y. Shih, I. A. Aksay, and R. Kikuchi, The Journal of Chemical Physics **86**, 5127 (1987).
[18] M. O. Robbins, K. Kremer, and G. S. Grest, The Journal of Chemical Physics **88**, 3286 (1988).
[19] K. Ito, K. Sumaru, and N. Ise, Phys. Rev. B **46**, 3105 (1992).
[20] H. Fudouzi and Y. Xia, Advanced Materials **15**, 892 (2003).
[21] C. P. Royall, M. E. Leunissen, A.-P. Hynninen, M. Dijkstra, and A. van Blaaderen, The Journal of Chemical Physics **124**, 244706 (2006).
[22] T. Kanai, T. Sawada, A. Toyotama, and K. Kitamura, Advanced Functional Materials **15**, 25 (2005).
[23] E. B. Sirota, H. D. Ou-Yang, S. K. Sinha, P. M. Chaikin, J. D. Axe, and Y. Fujii, Physical Review Letters **62**, 1524 (1989).
[24] R. Williams and R. Crandall, Physics Letters A **48**, 225 (1974).
[25] P. Chaikin, P. Pincus, S. Alexander, and D. Hone, Journal of Colloid and Interface Science **89**, 555 (1982).
[26] M. E. Leunissen, C. G. Christova, A.-P. Hynninen, C. P. Royall, A. I. Campbell, A. Imhof, M. Dijkstra, R. van Roij, and A. van Blaaderen, Nature **437**, 235 (2005).
[27] G. N. Smith, S. Alexander, P. Brown, D. A. J. Gillespie, I. Grillo, R. K. Heenan, C. James, R. Kemp, S. E. Rogers, and J. Eastoe, Langmuir **30**, 3422 (2014).
[28] R. Kemp, R. Sanchez, K. J. Mutch, and P. Bartlett, Langmuir **26**, 6967 (2010).
[29] P. J. Lu, E. Zaccarelli, F. Ciulla, A. B. Schofield, F. Sciortino, and D. A. Weitz, Nature **453**, 499 (2008).
[30] M. F. Hsu, E. R. Dufresne, and D. A. Weitz, Langmuir **21**, 4881 (2005).
[31] K. Mukherjee, S. P. Moulik, and D. C. Mukherjee, Langmuir **9**, 1727 (1993).
[32] M. B. Mathews and E. Hirschhorn, J. Colloid Sci. **8**, 86 (1953).
[33] I. D. Morrison, Colloids and Surfaces A: Physicochemical and Engineering Aspects **71**, 1 (1993).
[34] P. J. Lu, P. A. Sims, H. Oki, J. B. Macarthur, and D. A. Weitz, Opt. Express **15**, 8702 (2007).
[35] P. J. Lu, J. C. Conrad, H. M. Wyss, A. B. Schofield, and D. A. Weitz, Phys. Rev. Lett. **96**, 028306 (2006).
[36] P. J. Lu, M. Shutman, E. Sloutskin, and A. V. Butenko, Optics Express **21**, 30755 (2013).
[37] S. Alexander, P. M. Chaikin, P. Grant, G. J. Morales, P. Pincus, and D. Hone, The Journal of Chemical Physics **80**, 5776 (1984).
[38] E. Trizac, L. Bocquet, M. Aubouy, and H. H. von Grünberg, Langmuir **19**, 4027 (2003).
[39] F. Smallenburg, N. Boon, M. Kater, M. Dijkstra, and R. van Roij, The Journal of Chemical Physics **134**, 074505 (2011).
[40] W. L. Slattery, G. D. Doolen, and H. E. DeWitt, Phys. Rev. A **21**, 2087 (1980).
[41] S. Ichimaru, Rev. Mod. Phys. **54**, 1017 (1982).
[42] O. Vaulina and S. Khrapak, Journal of Experimental and Theoretical Physics **90**, 287 (2000).
[43] S. Hamaguchi, R. T. Farouki, and D. H. E. Dubin, Phys. Rev. E **56**, 4671 (1997).
[44] A.-P. Hynninen and M. Dijkstra, Phys. Rev. E **68**, 021407 (2003).